

The impact of typhoons on sediment connectivity: lessons learnt from contaminated coastal catchments of the Fukushima Prefecture (Japan)

Caroline Chartin, O. Evrard, J. Patrick Laceby, Yuichi Onda, Catherine Ottlé, Irène Lefevre, Olivier Cerdan

▶ **To cite this version:**

Caroline Chartin, O. Evrard, J. Patrick Laceby, Yuichi Onda, Catherine Ottlé, et al.. The impact of typhoons on sediment connectivity: lessons learnt from contaminated coastal catchments of the Fukushima Prefecture (Japan). Earth Surface Processes and Landforms, 2017, 42 (2), pp.306 - 317. 10.1002/esp.4056 . hal-01849975

HAL Id: hal-01849975
https://brgm.hal.science/hal-01849975

Submitted on 26 May 2020

HAL is a multi-disciplinary open access archive for the deposit and dissemination of scientific research documents, whether they are published or not. The documents may come from teaching and research institutions in France or abroad, or from public or private research centers.

L'archive ouverte pluridisciplinaire **HAL**, est destinée au dépôt et à la diffusion de documents scientifiques de niveau recherche, publiés ou non, émanant des établissements d'enseignement et de recherche français ou étrangers, des laboratoires publics ou privés.

The impact of typhoons on sediment connectivity: Lessons learnt from contaminated coastal catchments of the Fukushima Prefecture (Japan)

Caroline Chartin[1,2*], Olivier Evrard[1,*], J. Patrick Laceby[1], Yuichi Onda[3], Catherine Ottlé[1], Irène Lefèvre[1], Olivier Cerdan[4]

[1] *Laboratoire des Sciences du Climat et de l'Environnement (LSCE/IPSL) – Unité Mixte de Recherche 8212 (CEA, CNRS, UVSQ), Université Paris-Saclay, 91198-Gif-sur-Yvette Cedex, France*

[2] *Georges Lemaître Centre for Earth and Climate Research, Earth and Life Institute, Université Catholique de Louvain, 1348 Louvain-la-Neuve, Belgium*

[3] *Center for Research in Isotopes and Environmental Dynamics (CRIED), Tsukuba University, Tsukuba, Japan*

[4] *BRGM, ARN, 3 av. Claude Guillemin, BP 6009, 45060 Orléans, France*

**Corresponding authors: C.Chartin (caroline.chartin@uclouvain.be), O. Evrard (olivier.evrard@lsce.ipsl.fr)*

Keywords: storm events; soil erosion; flooding; sediment contamination; radiocesium

Abstract: Sediment connectivity characterizes the physical transfer of sediment through different geomorphic compartments in catchments due to sediment detachment, transport and deposition. Quantifying and modelling sediment connectivity is therefore a key prerequisite to improving our understanding of the dispersion of particle-borne contaminants, especially in catchments exposed to highly erosive climates. The objective of this study is to provide novel insights into typhoon impacts on sediment connectivity from hillslopes to rivers. The dispersion of particle-bound cesium-137 (^{137}Cs) was investigated in two coastal catchments draining the main contamination plume from the

Fukushima Daiichi Nuclear Power Plant accident. Five sampling campaigns were carried out from November 2011 to November 2015, after each typhoon season. The spatial and temporal evolution of ^{137}Cs contamination was investigated through the calculation of ^{137}Cs enrichment ratios in sediment relative to nearby soils. Rainfall erosivity (EI_{30}) associated with the main typhoons that occurred prior to each sampling campaign were computed, mapped, and finally used to improve a topographic-based Index of Connectivity. From 2011 to 2015, mean contamination levels in Mano and Niida catchments decreased from 11.9 kBq kg^{-1} to 3.3 kBq kg^{-1} and from 34.1 kBq kg^{-1} to 8.0 kBq kg^{-1}, respectively. Regional mean EI_{30} ranged from 262 MJ mm ha^{-1} h^{-1} for typhoon Jelawat (2012) to 1695 MJ mm ha^{-1} h^{-1} for typhoon Roke (2011). Typhoons Roke (2011) and Etau (2015) showed the highest connectivity from contaminated sources to the rivers, and induced a significant export of sediment to the ocean. In 2013 a slight increase in ^{137}Cs levels in river sediments occurred, likely resulting from the first step in decontamination works and the occurrence of two consecutive typhoons. Importantly, this research provides new insights into the connectivity of the main sources of sediments contaminated with radiocesium in Fukushima Prefecture and their temporal evolution, which will help with ongoing decontamination efforts.

1. Introduction

Sediment connectivity corresponds to the physical transfer of sediment from a source to a sink through sediment detachment, transport and deposition processes (Croke et al., 2013; Fryirs, 2013). This transfer is controlled by the type of sediment movement between catchment morphological compartments (i.e. within hillslopes, between hillslopes and river channels, and within river channels) (Bracken et al., 2013). Sediment connectivity encompasses two interrelated components: structural connectivity, which describes the physical links between compartments (i.e. morphology), and functional connectivity, which relates to the processes involved in sediment movements (e.g. erosion processes, transport, and energy vectors as water or wind) (Bracken et al., 2015). Sediment connectivity is the culmination of multiple processes, from particle detachment to deposition, where different systemic compartments may potentially act as a sediment source, pathway or sink (Wainwright et al., 2001; Parsons et al., 2006). Importantly, sediment connectivity changes in space

and time depending on the frequency-magnitude distribution of the detachment and transport processes, the spatial and temporal feedbacks between these processes, and the dominant mechanisms of sediment detachment and transport (Bracken et al., 2015). Although recent system-based research improved our understanding of sediment sources, transfer processes and sinks in catchments (e.g. Heckmann and Schwanghart, 2013; López-Vicente et al., 2013), sediment connectivity remains difficult to quantify, model and validate.

The Tohoku tsunami, induced by the March 2011 earthquake, impacted the Fukushima Daiichi Nuclear Power Plant (FDNPP) resulting in the largest release of radionuclides since the Chernobyl accident (Chino et al., 2011). Approximately 20% of these radionuclides were deposited within the Fukushima Prefecture (Kawamura et al., 2011; Kobayashi et al., 2013; Groëll et al., 2014). Currently, radiocesium (^{134}Cs and ^{137}Cs) presents the most serious short and long-term health risk (Kitamura et al., 2014; Saito et al., 2015). In June 2011, soils characterized by ^{137}Cs activities exceeding 100 kBq m^2 covered ~3000 km² in the region (MEXT, 2011). As radiocesium is strongly-bound to fine soil particles (i.e. clays and silts) (Tamura et al., 1964; Motha et al., 2002), the transfer of this contaminant from hillslopes to rivers is likely to be strongly influenced by sediment connectivity between catchment compartments.

The Fukushima Prefecture is characterized by high-relief topography and is subject to two main seasonal hydro-sedimentary regimes; spring snow melts and wet summers often typified by typhoon events known to produce catastrophic floods in tropical areas (Imamure and Van To, 1997; Cheng et al. 2005). The succession of these seasonal events leads to the erosion of contaminated soils and then to the export of radioactive material to the coastal plains (Chartin et al., 2013; Evrard et al. 2013). In particular, typhoon Roke (September 2011) resulted in elevated radiocesium concentrations sampled in suspended riverine material in the Fukushima Prefecture (Nago et al., 2013; Ueda et al., 2013; Mouri et al., 2014). Most of the rivers monitoring devices were damaged during the earthquake and tsunami, and river monitoring was only operational in the Abukuma River basin (5172 km²) that drains moderately contaminated soils. For this basin, more than 60% of the total radiocesium flux transported between August 2011 and May 2012 occurred during typhoon Roke (Yamashiki et al., 2014).

Recently, several river monitoring devices were also damaged during typhoon Etau in September 2015.

To counter the lack of river monitoring devices, alternative methods of tracking the contamination dispersion from hillslopes to rivers channels have been developed within coastal catchments draining the pollution plume. Sediment fingerprinting techniques used the spatial pattern of radioactive fallout (i.e., the variable ^{110m}Ag:^{137}Cs activity ratio) in soils to trace the export of riverine sediment (Chartin et al., 2013; Lepage et al., 2014a). Another technique consisted of measuring radioactive dose rates on soils and recently deposited river sediments (e.g. mud drapes on channel-bed sand) (Evrard et al., 2013; Evrard et al., 2014). This showed that the succession of the hydro-sedimentary events (i.e. typhoons and snowmelt runoff) led to the rapid decrease of radiation dose levels in river sediment in 2011-2012, and an increase after the 2013 typhoons due to renewed soil erosion. These tracing approaches provide complementary methods to characterise sediment connectivity between hillslopes and rivers channels in the absence of sediment monitoring devices, but a method to quantify spatial variations of sediment connectivity in time is still lacking.

The development of geomorphometric indices by means of GIS-based methods provides a way to identify and delineate areas with potential erosion and deposition, and dominant pathways between catchment compartments, contributing to sediment connectivity assessment in various contexts (e.g. Lane et al., 2009; Heckmann and Schwanghart, 2013). In ungauged coastal catchments of Fukushima Prefecture, a connectivity index identified the most potential contributive source areas of contaminated sediments (i.e. croplands located in valley bottoms and coastal plains) (Chartin et al., 2013). However, this index was originally designed to assess connectivity based on landscape information only (i.e. morphology and land cover), mainly describing the structural component of sediment connectivity without an effective integration of rainfall event characteristics, a functional component of sediment connectivity (Borselli et al., 2008). The principal limitation of this approach is that it only describes an intrinsic property of the landscape that is independent of the forcing events. In areas characterized by temperate climate regimes or for long-term average connectivity assessments, this limitation is acceptable. However in the context of tropical areas where the forcing events can differ by several

orders of magnitude, the amplitude of the transport agent may solicit different levels of connectivity and therefore imply very different hydro-sedimentary dynamics.

In this context, the objective of the paper is to provide novel insights into typhoon impacts on spatial and temporal evolution of sediment connectivity in coastal catchments contaminated with radiocesium in the Fukushima Prefecture (Japan). . First, the examination of five sediment sampling campaigns after each typhoon season since the FDNPP accident, from 2011 to 2015, provides a foundation for understanding sediment connectivity through the calculation of ^{137}Cs enrichment ratios (ER). Second, spatial variability of typhoon rainfall erosivity is studied for the most intensive typhoons that occurred prior to each sampling campaign. Finally, a topography-based index of connectivity is refined by integrating typhoon event rainfall erosivity as functional connectivity parameter, and comparing it to the ^{137}Cs ER. This research provides more understanding on the impact of typhoons on radiocesium transfer necessary for improving the management of post-accident radiocesium fallout in the Fukushima region.

2. Materials and methods

2.1. Study area

Most of the terrestrial fallout from the FDNPP accident occurred over the eastern part of the Fukushima Prefecture (Fig. 1). Soil contamination > 10 kBq kg^{-1} of ^{137}Cs occurred mostly within small catchments (< 700 km^2) draining to the Pacific Ocean, with the highest contamination levels in the coastal mountain range located northwest of the FDNPP. These coastal catchments are typical for Japan, dominated by steep forested hillslopes in upstream mountainous areas (up to 1000 m elevation), and by paddy fields and built-up areas in valley bottoms and coastal plains. River profiles are short, steep and strongly incised due to the geomorphological and hydrological contexts with the Japan archipelago being long and narrow, geologically young, tectonically active, and subject to a wet climate. Japanese catchments are frequently subject to heavy rainfall events (i.e. tropical storms and typhoons) (Laceby et al., 2016) likely leading to short-duration floods with high concentrations in

130 contaminated sediments (Yamaguchi et al., 2014; Evrard et al., 2015). Moreover, the ratio of bedload
131 to total load transported by Japanese rivers can reach 0.6 to 0.8 (e.g. Ohmori, 1991; Oguchi, 1997).

132 The climate in the study area is characterized by a hot and humid summer with monsoonal activity in
133 June-July and convective storms and an active typhoon season occurring mainly from July to October.
134 The region receives ~1420 mm y^{-1} of precipitation and rainfall erosivity is 3696 MJ mm ha^{-1} h^{-1} yr^{-1}
135 (Laceby et al., 2016) with the majority of precipitation (60%) and rainfall erosivity (86%) occurring
136 between June and October (Fig. 2). Typhoons are responsible for 22% of the annual precipitation (422
137 mm yr^{-1}) and 40% of the annual rainfall erosivity (1462 MJ mm ha^{-1} h^{-1} yr^{-1}) (Laceby et al., 2016). The
138 typhoons that occurred in the study area right prior each sampling campaign related to this study are
139 identified in Figure 2: typhoon Roke (2011), typhoon Jelawad (2012), typhoons Wipha and Francisco
140 (2013), typhoons Phanfone and Vongfong (2014), and typhoon Etau (2015).

141 Based on the geomorphological and climatic contexts of the eastern region of the Fukushima
142 Prefecture, two representative coastal catchments were investigated, (i.e. the Mano and Niida
143 catchments), covering ~450 km^2 North West of the FDNPP (Fig. 1). These steep short rivers originate
144 in the coastal mountain range, from an upstream altitude of 700 to 900 m a.s.l and drain into the
145 Pacific Ocean (Fig. 3a). The upstream sections of the Mano and Niida catchments are the most
146 contaminated with ^{137}Cs, with contamination decreasing downstream towards the coastal plain (Fig. 1)
147 (Chartin et al., 2013). The three main land uses, forests (deciduous and evergreen), croplands
148 (predominantly rice paddies) and built-up areas, cover 73%, 12% and 15% of the study area
149 respectively (Fig. 3b).

150 ## 2.2. Enrichment ratios (ER) in ^{137}Cs of river drape sediments

151 Lag deposit sediment samples (i.e. mud drapes deposited on channel-bed sand) were collected along
152 the main rivers draining the Mano and Niida catchments and some of their major tributaries after each
153 typhoon season between 2011 and 2015. At each sampling site, five to ten surface scrapes of deposited
154 sediment, collected along a 5 m river reach with a plastic spatula, were composited into one sample.
155 Upon returning to the laboratory, the samples were oven-dried (60 °C) for 48 h and then dry-sieved

(<2 mm). These samples were then ground to a fine powder, weighed, packed into 15 ml pre-tared polyethylene containers and sealed airtight prior to analyses.

^{137}Cs activities were determined by gamma spectrometry using low-background coaxial N- and P-types HPGe detectors. Counting time of soil and sediment samples varied between 3×10^4 and 8×10^4 s. The ^{137}Cs activities were measured at the 661 keV emission peak; errors reached ca. 5% at the 95% confidence level. All measured counts were corrected for background levels measured at least every 2 months as well as for detector and geometry efficiencies. Results were systematically expressed in Bq kg^{-1} of dry weight. Counting efficiencies and quality assurance were conducted using certified International Atomic Energy Agency (IAEA) reference materials prepared in the same containers as the samples. All radionuclide activities were decay-corrected to March 15, 2011.

The ^{137}Cs ER provides a quick and robust indication of the magnitude of ^{137}Cs contamination of the sediments compared with the local background contamination of soils. Hence sediments either have enriched (ER > 1) or depleted (ER < 1) ^{137}Cs activities relative to their most proximal sources depending on source and sink dynamics for nearby soil sources areas. ER values were calculated with all activities decay-corrected to March 15, 2011, as follows (Eq .1):

$$ER = \frac{^{137}Cs\ activity\ \left(\frac{Bq}{kg}\right) in\ the\ sediment\ sample}{^{137}Cs\ background\ activity\ (Bq/kg)\ in\ nearby\ soil\ sources} \quad (1)$$

The ^{137}Cs background activity in soils was determined for the whole study area through a mapping procedure based on a set of 2200 observations sampled in June and July 2011 and provided by the Japanese Ministry of Education, Culture, Sports, Science and Technology (MEXT). Detailed information about the Cs background mapping procedure is reported in Chartin et al. (2013). The ^{137}Cs background activity used in the ER calculation (eq. 1) was the mean valuepredicted for pixels located under cropland in the 100 m² area surrounding each of the river sampling sites.

2.3. Principles of the connectivity index

The connectivity index (IC) developed by Borselli et al., (2008) originally depicts the general structural connectivity that potentially occurs between different parts of a catchment (i.e. sources and

sinks). The basic form of the connectivity index is a ratio between an upslope component (D_{up}) and a downslope component (D_{dn}; Borselli et al., 2008):

$$IC = log_{10}(\frac{D_{up}}{D_{dn}}) \quad (2)$$

The IC value is defined in the range of -∞ ; +∞, with the higher the IC values indicating a lower potential for sediment produced upslope to be deposited in nearest downstream sinks. The upslope component (D_{up}) corresponds to the potential that sediment produced in the upslope contributing area be routed to the considered downstream pixel area. D_{up} is estimated as follows:

$$D_{up} = \sqrt{A}\,\overline{S}\,\overline{W} \quad (3)$$

Where A is the upslope contributing area (m²), $\overline{S}$ is the average slope gradient (m/m) of the upslope contributing area, and $\overline{W}$ is the average weighting factor of the upslope contributing area (see § 2.5). The downslope component (D_{dn}) characterizes the potential that the sediment, which is routed through the considered pixel area, has to be then transported downstream to the nearest sink along the flow path. D_{dn} is estimated as follows:

$$D_{dn} = \sum_i \frac{d_i}{S_i W_i} \quad (4)$$

Where d_i is the length of the flow path along the i^{th} cell according to the steepest slope (m), S_i and W_i are the slope gradient and the weighting factor of the i^{th} cell respectively.

2.4. Refinement to the index of sediment connectivity

Three changes were made to the model depicted above: i) thresholds were applied to the slope factor to adapt the model to the context of mountainous catchments (Cavalli et al., 2012), ii) the C-factor, as defined in the USLE equation (Wischmeier and Smith, 1978; Renard et al., 1997) and introduced in the calculation of the first version of the index (Borselli et al., 2008), was used as a weighting factor but was adapted from one typhoon event to another accordingly to the observed evolution of vegetation cover, and iii) a rainfall erosivity weighting (Rt) factor was added as a second weighting factor to account for the specificity of typhoon events (i.e., event frequency, intensity and rainfall

amount). In this work, we focused on the main typhoons that occurred prior to each sampling campaign (i.e., Roke in 2011, Jelawad in 2012, Wipha and Francisco in 2013, Phanfone and Vongfong in 2014 and Etau in 2015) (Fig. 2). Two events were chosen for years 2013 and 2014 as these events occurred very close in time. So, the revised version of the IC model (IC_{rev}) used here corresponds to the following ratio:

$$IC_{rev} = log_{10}\left(\frac{\sqrt{A}\,\bar{S}\,\bar{C}\,\overline{R_t}}{\frac{d_i}{\sum_i S_i\,C_i\,Rt_i}}\right) \quad (5)$$

Slope factor

Morphometric parameters (A, S) were derived from a Digital Elevation Model (DEM) with a 10 m resolution provided by the Geospatial Information Authority of Japan (GSI) from the Ministry of Land, Infrastructure, Transport and Tourism (http://www.gsi.go.jp/; Fig. 1). This DEM was derived from LIDAR airborne monitoring surveys. A minimum threshold value of 0.005 m/m was applied to the slope layer to avoid infinite values in Eq. 4 (Borselli et al., 2008), and a maximum threshold value of 1 m/m was applied to avoid a bias (very high IC values) on the steepest slopes (Cavalli et al., 2012).

Cover factor

The Cover factor (C-factor) accounts for the effects of plants, soil cover, soil biomass, and soil disturbing activities on soil erosion (i.e. particle detachment)(Wischmeier and Smith, 1978; Renard et al., 1991; Renard et al., 2007). It also accounts for the effects of vegetation on water infiltration. Values were determined based on terrain observations made during each fieldwork campaign and data found in the literature (Kitahara et al., 2000; Shiono et al., 2002; Yoshikawa et al., 2004). A C-factor value of 0.01 was applied to forested areas, and 1 to bare soils and built-up areas for the experiment period. Values for cropland areas were 0.38 for 2011, 0.17 for 2012 and 0.04 for the remaining years. These values were applied to land use classes determined by a multitemporal and multispectral classification of images from SPOT-4 and SPOT-5 satellites (Chartin et al., 2013).

Rainfall erosivity factor

To calculate rainfall erosivity, precipitation data recorded in 10 minute intervals between 2011 and 2015 was downloaded from 40 monitoring stations located within 100 km of the FDNPP that are operated by Japan Meteorological Agency's Automated Meterological Data Acquisition System (AMeDAS). The Rainfall Intensity Summarisation Tool (RIST) software (USDA, 2013) was used to determine the rainfall erosivity (EI_{30}) of each typhoon (Laceby et al., 2016). Rainfall erosivity is a product of the energy (E) of the rainfall event and its maximum 30-minute intensity (I_{30}) (Renard and Freimund, 1994). RIST was used to calculate the rainfall erosivity for 3 days before and 3 days after each typhoon event to ensure that all the potential rainfall erosivity associated with the event was included.

The criteria used to identify the erosive events were: 1) cumulative rainfall of an event was >12.7mm; and 2) rainfall accumulations <1.27mm for a 6 hour period separated events into two different periods. These criteria isolated the period of the typhoon events for which EI_{30} were calculated via:

$$EI_{30} = \left(\sum_{r=1}^{O} e_r v_r\right) I_{30} \quad (6)$$

with e_r representing rainfall energy per unit depth of rainfall in MJ ha^{-1} mm^{-1}, v_r is the volume of rainfall (mm) during a given time period (r), and I_{30} is the maximum rainfall intensity over a 30 minute period of the rainfall event (mm h^{-1}). For each time interval, e_r is calculated as:

$$e_r = 0.29\left[1 - 0.72^{(-0.05 i_r)}\right] \quad (7)$$

with i_r being the rainfall intensity for the time interval (mm h^{-1}) (Brown and Foster, 1987).

The EI_{30} was then mapped based on the values computed for all the stations located within the 100 km area around the FDNPP (see § 2.6). Then, we computed the rainfall weighing (R_t) factor as follows:

$$R_t = \frac{EI_{30}}{EI_{30max}} \quad (8)$$

Where EI_{30max} is the maximum EI_{30} value predicted amongst the five considered typhoon events within the restricted area of the study catchments. This normalization of the R_t factor allows to avoid bias induced by high EI_{30} values, and to provide same range values as for S and C factors.

2.5. Mapping the rainfall erosivity factor

The EI_{30} values were used to compute maps of typhoon erosivity at a resolution of 250 m over the eastern part of the Fukushima Prefecture. A regression approach, based on relationships established between the EI_{30} data and spatially distributed covariates, was used to produce these maps. The covariates used in the modelling procedure were morphometric attributes (elevation, slope and aspect), climatic data (monthly mean rainfall and mean temperature), distance to the coast and geographical coordinates. Detailed information about the source data and the computation of the covariates layers is provided in Laceby et al. (2016).

The spatially continuous covariates were rescaled at a 250 m resolution in ArcGIS10 (ESRI, 2011) with bilinear interpolation. The spatial distribution of typhoon rainfall erosivity in the eastern part of the Fukushima prefecture was then modelled with Generalized Additive Models (GAM; Hastie ad Tibshirani, 1986). GAMs were fitted on five datasets, i.e., EI_{30} values computed for typhoon Roke (2011), typhoon Jelawad (2012), typhoon Etau (2015), and sums of EI_{30} values computed for typhoons Wipha and Francisco (2013), and for typhoons Phanfone and Vongfong (2014). The GAM technique is a generalization of linear regression models in which the coefficients can be a set of smoothing functions, accounting then for the non-linearity that could exist between the dependent variable and covariates. GAM specifies a distribution for the conditional mean μ(Y) and a link function g relating this latter to an additive function of the covariates:

$$g[\mu\,(Y)] = \alpha + f_1X_1 + f_2X_2 + \cdots + f_pX_p \quad (9)$$

where Y is the dependent variable, X1,X2,…Xp represent the covariates and the fi's the smooth (non-parametric) functions.

Based on EI_{30} data computed for the 40 rain stations, GAMs were fitted to spatially model the rainfall erosivity of the selected typhoons over the eastern part of Fukushima prefecture including the two investigated catchments (Fig. 1). A Gaussian distribution model incorporated the conditional mean $\mu(Y)$ and a log-linear link function $g(\mu) = \log(\mu)$ was implemented due to the predominant logarithmic distribution of the data. The GAM models were built using regression splines, and the smoothing parameters were estimated by penalized Maximum Likelihood to avoid an over-fitting (Wood, 2001). A leave-one-out cross-validation procedure was applied to each fitted models, and then mean error (ME) and root mean square error (RMSE) were calculated to quantify their goodness of fit.

3. Results and discussion

3.1. Evolution of radioactive contamination in river drape sediments

Evolutions of ^{137}Cs contents and ^{137}Cs ER of river sediment deposits were examined to investigate the evolution of sediment connectivity between contaminated hillslopes and river channels (Figs. 4 and 5). Mean contamination levels of the sediments in the Niida river were 2 to 3 times higher than in the Mano river (Fig. 4). This reflects the differences observed between the contamination background of soil sources within the two catchments (Fig. 1). Mean sediment contamination decreased substantially from 2011 to 2012 and from 2014 to 2015, with a more slight decrease from 2012 to 2013 (Fig. 4). From 2011 to 2015, mean contamination levels in Mano catchment and Niida catchment decreased from 11.9 kBq kg^{-1} (SD 6.8; n=5) to 3.3 kBq kg^{-1} (SD 2.0; n=18) and from 34.1 kBq kg^{-1} (SD 29.0; n=16) to 8.0 kBq kg^{-1} (SD 5.5; n=19), respectively. The only exception is a slight increase of mean sediment contamination observed from 2012 to 2013 in the Niida River (from 17.7 kBq kg^{-1} (SD 14.5; n=18) to 20.4 kBq kg^{-1} (SD 15.3; n=22)).

Following the first typhoon season occurring after the FDNPP accident, ER values were predominantly greater than 1.5 in both catchments (red dots in Fig. 5) confirming dynamic sediment regimes that connected hillslopes to rivers, and that a massive export of contaminated particles occurred. This observation can locally be reversed in the upstream part of catchments (river sediments

had lower ^{137}Cs activities than nearby soils), especially where valley bottoms are narrow and uncultivated and, consequently, scarce sediment source areas (Fig. 3).

From 2011 to 2012, ER values of most samples from mountainous upstream areas (brown to white areas in Figure 5) decreased (median value of ER evolved from 1.8 to 0.7 from 2011 to 2012). A slight increase of ER values occurred in 2013 (median ER = 0.8) just after two consecutive typhoons (Wipha and Francisco) for most of the samples analysed in both catchments, confirming the observations that hillslope soil erosion processes were renewed (Evrard et al., 2014). From 2013 to 2015, ER values of most samples from both catchments decreased (median ER = 0.4 for year 2015). A new element to take into account for this period is the very rapid progress of the decontamination works that have remobilized contaminated material by erosion processes that were formerly protected by the post-accident vegetation regrowth, and then rapidly removed the contamination from the surface of the areas covered by non-permanent vegetation.

3.2. Typhoon characteristics and mapping

Erosivity of the most intense typhoons that occurred prior to each sampling campaign was computed for the meteorological stations located within the 100 km area around FDNPP (Table 1). Mean EI_{30} values ranged from 262 MJ mm ha^{-1} h^{-1} (SD 197; n=36) for typhoon Jelawat in 2012 to 1695 MJ mm ha^{-1} h^{-1} (SD 1066; n=39) for typhoon Roke in 2011. GAMs were fitted to the observed values. Validation procedure of the models resulted in R^2 varying between 0.83 and 0.95, and predicted values showed similar distributions to those of observed values (Table 1).

The rainfall erosivity maps (EI_{30} in MJ mm ha^{-1} h^{-1}) are depicted at two different scales, the 100 km buffer area around FDNPP and the two investigated catchments in Figure 6A and Figure 6B, respectively. At the regional scale, all the typhoons except Jelawat (2011) showed the same general spatial pattern with typhoon erosivity strongly decreasing from the coast (east) to the inland areas (west) (Fig. 6A). This reflects the role of the Pacific Ocean on driving tropical storms and typhoons. Accordingly, the coastal plain and coastal mountainous ranges, including the FDNPP and a large part of the contamination plume with high levels of ^{137}Cs contamination, were submitted to greater typhoon

erosivity than the less contaminated Abukuma River valley. This spatial pattern was also observed at the regional scale for monthly mean rainfall erosivity during wet and typhoon season (from June to October), i.e. during the most erosive annual period (Laceby et al., 2016).

At the scale of the two investigated catchments, rainfall erosivity decreased from the coastal plains to the upslope mountainous areas for the typhoon Roke (2011), typhoons Wipha and Francisco (2013) and typhoons Phanfone and Vongfong (2014) (Fig. 6B). Typhoons Jelawat (2012) and Etau (2015), the least and the most erosive events respectively, had a positive gradient of rainfall erosivity from the coast to the mountain range. According to the typhoon erosivity maps, the Mano and Niida catchments were submitted to rather similar rainfall erosivity for each individual event, e.g. mean EI_{30} was 653 MJ mm ha^{-1} h^{-1} (SD 146) and 608 MJ mm ha^{-1} h^{-1} (SD 209) for Mano and Niida catchments respectively during the Wipha/Francisco event of 2013.

The relative intensity of the different typhoon events at the catchment scale appeared quite different from the one observed at the regional scale. According to the observed and predicted EI_{30} values (Table 1), typhoon Roke (2011) and typhoon Etau (2015) had similar mean erosivities at the regional scale, i.e. mean observed values of 1695 MJ mm ha^{-1} h^{-1} and 1581 MJ mm ha^{-1} h^{-1} respectively. However, the SD was higher for typhoon Etau (SD 1577) than for typhoon Roke (SD 1066) indicating, in these cases of right skewed distributions, that the erosivity magnitude of typhoon Etau had locally reached higher values than maximum values observed for typhoon Roke. Indeed, mean predicted values for typhoon Etau (2015) were two times higher than those for typhoon Roke (2011) at the scale of the two studied catchments. For example, we predicted mean EI_{30} values of 4299 MJ mm ha^{-1} h^{-1} (SD 1702) for Typhoon Etau and 2099 MJ mm ha^{-1} h^{-1} (SD 520) for Typhoon Roke (Table 2). This could possibly be explained by the characteritiscs of these different events (e.g. path, speed, intensity).

3.3. Revised Index of Connectivity (IC_{rev}) and relationship with ^{137}Cs Enrichment Ratios (ER)

The EI_{30} maps were used to compute the revised Index of Connectivity (IC_{rev}) for the five typhoon events (Fig. 7). The IC_{rev} maps corresponding to the different typhoon events all identify croplands and

350 built up areas as the most potentially connected sediment source areas to the river network. However,
351 the calculated connectivity indices display very different values depending on the evolution of the
352 vegetation cover (C-factor), but most importantly, on the differences in rainfall erosivity between
353 events (Table 3). Although both events were characterized by equivalent C-factors, IC_{rev} values were
354 higher for the more intense typhoon Etau (mean of -7.2; SD 1.5 in Mano catchment) than for the less
355 intense typhoon Wipha and Francisco (mean of -8.7; SD 1.4 in Mano catchment) (Table 2, Fig. 7). In
356 addition, maps of the IC_{rev} show variations in sediment connectivity reflecting the spatial
357 characteristics of the event erosivity as depicted in Figure 6B. For example, the connectivity index
358 associated with typhoon Etau (2015) increased from coastal plain to upstream mountainous areas
359 while, on the contrary, connectivity index computed for typhoons Phanfone and Vongfong (2014)
360 decreased in this same direction.

361 We compared the index values computed for the five typhoons events to ER values (Fig. 8). For all the
362 events, except typhoons Phanfone and Vongfong in 2014 in the Niida catchment, a negative
363 exponential relation was observed between IC_{rev} and ER values. Accordingly, these results clearly
364 indicate that the higher the connectivity, the lower the potential for contaminated sediment, from
365 nearby source areas, to be deposited at locations sampled downstream (Borselli et al., 2008).

366 Coefficients of correlations between IC_{rev} and ER values ranged between 0.01 in Mano catchment for
367 typhoons Phanfone and Wongfong (2014) to 0.44 in Niida catchment for typhoon Etau (2015; Fig. 8).
368 A coefficient of correlation of 0.01 was also observed in Mano catchment for typhoon Roke (2011)
369 but cannot be considered as representative considering the low number of observed sites (n=5). The
370 strongest relationships between IC_{rev} and ER values were observed for the two most erosive typhoons
371 (Roke and Etau) with the Mano and Niida catchments having a R^2 of 0.29 and 0.44 respectively for
372 typhoon Etau in 2015. Typhoon Roke was the first major typhoon after the FDNPP accident leading to
373 the widespread erosion of initially contaminated soil sources and their export to the Pacific Ocean
374 (Fig. 4; Yamashiki et al., 2014). Etau was the most intense typhoon that occurred at the Mano and
375 Niida catchments scale since the accident likely leading to the flush of recently eroded material and
376 also temporary stored contaminated material within the channels to the Pacific Ocean (Fig. 4). The

Mano catchment showed mainly lower coefficients of correlation than Niida catchment except for the typhoon Wipha and Francisco in 2014. The Mano catchment was originally less contaminated and had much more narrow upstream valley bottoms and also less cultivated areas than in Niida catchment (i.e. less potential connected source areas) (Fig. 1; Fig. 3). This may explain why the relationships observed between IC_{rev} and ER values for Mano catchment were lower than in the Niida catchment.

The results are contrasted, particularly for the less intense rainfall events. Even though, it is now well accepted that rainfall erosivity has a strong influence on sediment connectivity, sediment detachment, transport and deposition processes are complex and subject to multiple forcing that interact non-linearly in time and space. In our context, among other factors, we can cite the spatial heterogeneity of the background contamination (including the progressive decontamination works), the multiplicity of erosion processes that can either affect contaminated surface materials (e.g. surface hillslope erosion) or non-contaminated materials (mass movement, bank erosion), or the complex succession of events of different magnitude that imply progressive deposition and re-entrainment processes. This complexity explains that the relationship between connectivity and rainfall erosivity can only be qualified for the more intense typhoons that occurred in the area: Roke and Etau, but which also demonstrates the importance to incorporate the characteristics of the forcing agents when modelling water and sediment connectivity.

Future research should strive to improve ER and ICrev modelling approaches and examine the impact and limitations of these potential factors that may be influencing the relationship between ER values and connectivity. Importantly, this research represents a significant first step towards incorporating the erosivity of rainfall directly into sediment connectivity indices, which is important in regions similar to Fukushima, where nearly half of the rainfall erosivity is derived from major rainfall events.

4. Conclusion

Typhoons are major drivers for soil erosion, and also for potential dispersion and downstream transfer of particles bound contaminants. Here, the downstream dispersion of sediments contaminated with

radiocesium was investigated after five consecutive typhoon seasons (from 2011 to 2015) in two ungauged catchments draining the main contamination plume of Fukushima Prefecture.

From 2011 to 2015, mean contamination levels in Mano and Niida catchments decreased from 11.9 kBq kg^{-1} to 3.3 kBq kg^{-1} and from 34.1 kBq kg^{-1} to 8.0 kBq kg^{-1}, respectively. Mean sediment contamination strongly decreased early after the accident, from 2011 to 2012, and then, to a lesser extent, between 2014–2015. In particular, it was demonstrated that the catchment systems and their contaminated sediment connectivity had higher correlations for events with the highest rainfall erosivity. Indeed, the highest correlations between the revised Index of Connectivity (ICrev) and the sediment ER in ^{137}Cs were observed for the most erosive typhoons, i.e. Roke in 2011 and Etau in 2015. These two typhoons resulted in a high level of connectivity between sources of eroded contaminated particles and the river systems, and contributed greatly to the export of contaminated material to the Pacific Ocean. In 2013, a slight increase in ^{137}Cs levels in river sediments was observed, likely resulting from the beginning of the decontamination works and the occurrence of two consecutive typhoons (Wipha and Francisco). From 2013 to 2015, the typhoon events resulted in the dilution of the ^{137}Cs signal in river sediments by inputs of different non-contaminated subsoil sources and decontaminated surface sources relative to contaminated surface source contributions. Although it remains difficult to fully validate sediment connectivity models with complex metrics of radiocesium downstream migration (ER values), this interpretation, based on both ICrev and ER values, demonstrates the importance of including individual storm erosivity and detailed vegetation cover information when quantifying sediment connectivity indices. These results indicate that the calculation of ICrev may provide a very useful tool to improve the estimation of particle-borne contaminant fluxes during extreme events, particularly in ungauged catchments.

Acknowledgements:

This work has been supported by the French National Research Agency (ANR) in the framework of AMORAD project (ANR-11-RSNR-0002). Assistance of Jeremy Patin, Philippe Bonté, Hugo Lepage and Hugo Jaegler for fieldwork was greatly appreciated.

433 REFERENCES:

434 Borselli L, Cassi P, Torri D. 2008. Prolegomena to sediment and flow connectivity in the landscape: a
435 GIS and field numerical assessment. *Catena* **75** : 268–277.

436 Bracken LJ, Turnbull L, Wainwright J, Bogaart P. 2015. Sediment connectivity: a framework for
437 understanding sediment transfer at multiple scales. *Earth Surface Processes and Landforms* **40**: 177-
438 188.

439 Bracken LJ, Wainwright J, Ali GA, Tetzlaff D, Smith MW, Reaney SM, Roy AG. 2013. Concepts of
440 hydrological connectivity: research approaches, pathways and future agendas. *Earth Science Reviews*
441 **119**: 17–34.

442 Cavalli M, Trevisani S, Comiti F, Marchi L, 2012. Geomorphic assessment of spatial sediment
443 connectivity in small Alpine catchments. *Geomorphology* **188**: 31-41.

444 Chartin C, Evrard O, Onda Y, Patin J, Lefèvre I, Ottlé C, Ayrault S, Lepage H, Bonté Ph. 2013.
445 Tracking the early dispersion of contaminated sediment along rivers draining the Fukushima
446 radioactive pollution plume. *Anthropocene* **1**, 23–34.

447 Cheng JD, Huang YC, Wu HL, Yeh, JL, Chang CH. 2005. Hydrometeorological and landuse
448 attributes of debris flows and debris floods during typhoon Toraji, July 29-30 2001 in central Taïwan.
449 *Journal of Hydrology* **306(1-4)**: 161-173.

450 Chino M, Nakayama H, Nagai H, Terada H, Katata G, and Yamazawa H. 2011. Preliminary
451 estimation of release amounts of ^{131}I and ^{137}Cs accidentally discharged from the Fukushima Daiichi
452 nuclear power plant into the atmosphere. *Journal of nuclear science and technology* **48(7)**: 1129-1134.

453 Croke J, Fryirs K, Thompson C. 2013. Channel–floodplain connectivity during an extreme flood
454 event: implications for sediment erosion, deposition, and delivery. *Earth Surface Processes and*
455 *Landforms* **38(12)**: 1444–1456.

456 ESRI. 2011. ArcGIS Desktop: Release 10. Redlands. Environmental Systems Research Institute, CA.

Evrard O, Chartin C, Onda Y, Patin J, Lepage H, Lefèvre I, Ayrault S, Ottlé C, Bonté Ph. 2013. Evolution of radioactive dose rates in fresh sediment deposits along coastal rivers draining Fukushima contamination plume. *Scientific Reports* **3**, 3079.

Evrard O, Chartin C, Onda Y, Lepage H, Cerdan O, Lefèvre I, Ayrault S. 2014. Renewed soil erosion and remobilisation of radioactive sediment in Fukushima coastal rivers after the 2013 typhoons. *Scientific Reports* **4**, 4574.

Evrard O., Laceby J. P., Lepage H., Onda Y., Cerdan O., Ayrault S. 2015. Radiocesium transfer from hillslopes to the Pacific Ocean after the Fukushima Nuclear Power Plant accident: A review. *Journal of Environmental Radioactivity* **148**: 92–110.

Fryirs K. 2013. Connectivity in catchment sediment cascades: a fresh look at the sediment delivery problem. *Earth Surface Processes and Landforms* **38(1)**: 30–46.

Fukushima River Basin Comprehensive Information System. 2013.http://kaseninf.pref.fukushima.jp/gis/

Groëll J, Quélo D, Mathieu A. 2014. Sensitivity analysis of the modelled deposition of ^{137}Cs on the Japanese land following the Fukushima accident. *International Journal of Environment and Pollution* **55(1)**: 67-75.

Hastie T, and Tibshirani R. 1986. Generalized additive models. *Statistical science* **1(3)**: 297-310.

Heckmann T and Schwanghart W. 2013. Geomorphic coupling and sediment connectivity in an alpine catchment exploring sediment cascades using graph theory. *Geomorphology* **182**: 89-103.

Hijmans RJ, Cameron SE, Parra JL, Jones PG,Jarvis A. 2005. Very high resolution interpolated climate surfaces for global land areas. *International Journal of Climatology* **25(15):** 1965-1978. DOI: 10.1002/joc.1276

Imamure F, Van To D. 1997. Flood and typhoon disasters in Viet Nam in the half century since 1950. *Natural Hazards* **15**: 71-87.Kawamura H, Kobayashi T, Furuno A, In T, Ishikawa Y, Nakayama T,

Shima S, Awaji T. 2011. Preliminary numerical experiments on oceanic dispersion of ^{131}I and ^{137}Cs discharged into the ocean because of the Fukushima Daiichi nuclear power plant disaster. *Journal of nuclear science and technology* **48(11)**: 1349-1356.

Kitahara H, Okura Y, Sammori T, Kawanami A. 2000. Application of the Universal Soil Loss Equation in mountainous forests in Japan. *Journal of Forest Research* **5**: 231-236.

Kitamura A, Yamaguchi M, Kurikami H, Yui M, Onishi Y. 2014. Predicting sediment and cesium-137 discharge from catchments in eastern Fukushima. *Anthropocene* **5**: 22-31.

Kobayashi T, Nagai H, Chino M, Kawamura H. 2013. Source term estimation of atmospheric release due to the Fukushima Dai-ichi Nuclear Power Plant accident by atmospheric and oceanic dispersion simulations: Fukushima NPP Accident Related. *Journal of Nuclear Science and Technology* **50(3)**: 255-264.

Kusakabe, M., Oikawa, S., Takata, H., and Misonoo, J. 2013 Spatiotemporal distributions of Fukushima-derived radionuclides in nearby marine surface sediments. *Biogeosciences* **10:** 5019–5030.

Laceby JP, Chartin C, Evrard O, Onda Y, Garcia-Sanchez L, Cerdan O. 2016. Rainfall erosivity in catchments contaminated with fallout from Fukushima Daiichi nuclear power plant accident. *Hydrology and Earth System Sciences* **20:** 1-16.

Laceby JP, Huon S, Onda Y, Vaury V, Evrard O. (in review) Tracing particulate matter sources in coastal catchments of the Fukushima Prefecture with carbon and nitrogen concentrations and stable isotope ratios. *Science of the Total Environment*

Lane SN, Reaney SM, Heathwaite AL. 2009. Representation of landscape hydrological connectivity using a topographically driven surface flow index: hydrological connectivity. *Water Resources Research* **480 45(8)**:W08423.

Lepage H, Evrard O, Onda Y, Chartin C, Lefèvre I, Ayrault S, Bonté P. 2014b. Tracking the origin and dispersion of contaminated sediments transported by rivers draining the Fukushima radioactive

505 contaminant plume. Proceedings of a symposium held in New Orleans, Louisiana, USA, (11–14
506 December 2014), *IAHS Publ*. **367**: 237-245.

507 Lepage H, Evrard O, Onda Y, Patin J, Chartin C, Lefèvre I, Bonté P, Ayrault S. 2014a. Environmental
508 mobility of 110mAg: lessons learnt from Fukushima accident (Japan) and potential use for tracking
509 the dispersion of contamination within coastal catchments. *Journal of Environmental Radioactivity*
510 **130**: 44–55.

511 López-Vicente M, Poesen J, Navas A, Gaspar L. 2013. Predicting runoff and sediment connectivity and
512 soil erosion by water for different land use scenarios in the Spanish Pre-Pyrenees. *Catena* **102:** 62-73.

513 Ministry of Education, Culture, Sports Science and Technology (MEXT). 2011. Preparation of
514 distribution map of radiation doses, etc. (Map of radioactive cesium concentration in soil) by MEXT.
515 http://radioactivity.mext.go.jp/en/contents/5000/4165/24/1750_083014.pdf.

516 Motha JA, Wallbrink PJ, Hairsine PB, Grayson RB. 2002. Tracer properties of eroded sediment and
517 source material. *Hydrological Processes* **16**: 1983–2000.

518 Mouri G, Golosov V, Shiiba M, Hori T. 2014. Assessment of the cesium-137 flux adsorbed to
519 suspended sediment in a reservoir in the contaminated Fukushima region in Japan. *Environmental*
520 *Pollution* **187C**: 31–41.

521 Nagao S, Kanamori M, Ochiai S, Tomihara K, Fukushi K, Yamamoto M. 2013. Export of ^{134}Cs and
522 ^{137}Cs in the Fukushima river systems at heavy rains by Typhoon Roke in September 2011.
523 *Biogeosciences* **10**: 6215–6223.

524 Ohmori H. 1991. Change in the mathematical function type describing the longitudinal profile of a
525 river through an evolutionary process. *Journal of Geology* **99:** 97-110.

526 Oguchi T., 1997. Late Quaternary sediment budget in alluvial-fan-source-basin systems in Japan.
527 *Journal of Quaternary Science* **12**: 381-390.

528 Parsons AJ, Brazier RE, Wainwright J, Powell DM. 2006. Scale relationships in hillslope runoff and
529 erosion. *Earth Surface Processes and Landforms* **31**: 1384–1393.

530 Renard KG, Foster GR, Weesies GA, McCool D, Yoder D. 1997. Predicting soil erosion by water: a
531 guide to conservation planning with the revised universal soil loss equation (RUSLE). USDA (eds).
532 Agriculture Handbook: Washington, 703.

533 Renard KG, Foster GR, Weesies GA, Porter JP. 1991. RUSLE: Revised universal soil loss equation.
534 *Journal of soil and Water Conservation* **46(1)**: 30-33.

535 Saito K, Tanihata I, Fujiwara M, Saito T, Shimoura S, Otsuka T, Onda Y, Hoshi M, Ikeuchi Y,
536 Takahashi F. 2015. Detailed deposition density maps constructed by large-scale soil sampling for
537 gamma-ray emitting radioactive nuclides from the Fukushima Dai-ichi Nuclear Power Plant accident.
538 *Journal of environmental radioactivity* **139**: 308-319.

539 Shiono T, Kamimura K, Okushima S, Fukumoto M. 2002. Soil loss estimation on a local scale for soil
540 conservation planning. *Japan Agriculture Research Quaterly* **36(3)**: 157-161.

541 Tamura T. 1964. Consequences of activity release: selective sorption reactions of cesium with soil
542 minerals. *Nuclear Safety* **5**: 262–268.

543 Thornton B, Ohnishi, S, Ura T, Odano N, Sasaki S, Fujita T, Watanabe T, Nakata K, Ono T, Ambe D.
544 Distribution of local 137Cs anomalies on the seafloor near the Fukushima Daiichi Nuclear Power
545 Plant, *Mar. Pollut. Bull*. **74**: 344–350.

546 Ueda S, Hasegawa H, Kakiuchi H, Akata N, Ohtsuka Y, Hisamatsu S. 2013. Fluvial discharges of
547 radiocesium from watersheds contaminated by the Fukushima Dai-ichi Nuclear Power Plant accident,
548 Japan. Journal of Environmental Radioactivity **118**: 96–104.

549 USDA. 2013. Rainfall Intensity Summarization Tool (RIST), United States Department of Agriculture
550 (USDA), Agriculture Research Service, National Sedimentation Laboratory, Oxford, Mississippi,
551 Version 3.88.

552 Wainwright J, Parsons AJ, Powell DM, Brazier RE. 2001. A new conceptual framework for
553 understanding and predicting erosion by water from hillslopes and catchments. In Ascough JC,
554 Flanagan DC (eds). Soil Erosion Research for the 21st Century. Proceedings of the International
555 Symposium, Thomas DSG (ed). American Society of Agricultural Engineers: St Joseph, MI; 607–610.

556 Wischmeier WH and Smith DD. 1978. Predicting rainfall erosion losses-A guide to conservation
557 planning. Predicting rainfall erosion losses-A guide to conservation planning. USDA (eds.).
558 Agriculture Handbook: Washington, 537.

559 Wood, S. N. 2001. mgcv: GAMs and generalized ridge regression for r. *R news* **1(2)**: 2-25.

560 Yamaguchi M., Kitamura A., Oda Y., Onishi Y. 2014. Predicting the long-term 137Cs distribution in
561 Fukushima after the Fukushima Dai-ichi nuclear power plant accident: a parameter sensitivity
562 analysis. *Journal of Environmental Radioactivity* **135**: 135–146

563 Yamashiki Y, Onda Y, Smith HG, Blake WH, Wakahara T, Igarashi Y, Matsuura Y, Yoshimura K.
564 2014. Initial flux of sediment-associated radiocesium to the ocean from the largest river impacted by
565 Fukushima Daiichi Nuclear Power Plant. *Scientific Reports* **4**, 3714.

566 Yoshikawa S, Yamamoto H, Hanano Y, Ishihara A. 2004. Hilly-land Soil Loss Equation (HSLE) for
567 evaluation of soil erosion caused by the abandonment of agricultural practices. *Japan Agricultural*
568 *Research Quaterly* **38(1)**: 21-29.

569

570 Table 1. Observed and predicted rainfall erosivity mean and standard deviation (SD) (EI_{30} in MJ mm ha^{-1} h^{-1}) for major events that occurred during each
571 typhoon season since the nuclear accident within the 100 km area around the FDNPP, and parameters describing performance of the GAMs used to map EI_{30}
572 in the area.

Typhoon event	Date	Number of stations	Observed EI_{30}		Predicted EI_{30}		Model performance		
			Mean	SD	Mean	SD	ME	RMSE	R^2
Roke	Sept. 8-22, 2011	39	1695	1066	1706	1005	11.6	289.0	0.89
Jelawat	Sept. 20 - Oct. 1, 2012	36	262	197	269	168	7.4	80.3	0.83
Wipha & Francisco	Oct. 9-26, 2013	39	549	317	551	298	2.1	80.8	0.89
Phanfone &Vongfong	Sept. 28 - Oct. 14, 2014	40	1034	759	1033	721	3.5	159.6	0.95
Etau	Sept. 6 - 9, 2015	40	1581	1577	1554	1489	-26.4	588.0	0.86

573

574 Table 2. Mean rainfall erosivity (EI_{30} in in MJ mm ha^{-1} h^{-1}) and standard deviation (SD) of major
575 events that occurred during each typhoon season since the FDNPP accident for Mano and Niida
576 catchments (statistics were computed by zonal statistics tool in ArcGis 10.3 and based on EI_{30} maps
577 presented in Figure 6B).

Typhoon event	Date	Mano catchment		Niida catchment	
		Mean EI_{30}	SD	Mean EI_{30}	SD
Roke	Sept. 8-22, 2011	2099	520	1826	646
Jelawat	Sept. 20 - Oct. 1, 2012	187	62	209	67
Wipha & Francisco	Oct. 9-26, 2013	653	146	608	209
Phanfone & Vongfong	Sept. 28 - Oct. 14, 2014	1469	941	1231	941
Etau	Sept. 6 - 9, 2015	4299	1702	4124	1602

578

579

580

581 Table 3. Mean revised Connectivity Index (IC_{rev}) and standard deviation (SD) of major events
582 occurred during each typhoon season since the FDNPP accident for the Mano and Niida catchments
583 (Statistics were computed by zonal statistics tool in ArcGis 10.3 and based on IC_{rev} maps presented in
584 Figure 7).

Typhoon event	Date	Mano catchment		Niida catchment	
		Mean iCrev	SD	Mean Icrev	SD
Roke	Sept. 8-22, 2011	-7.6	1.3	-7.8	1.4
Jelawat	Sept. 20 - Oct. 1, 2012	-9.8	1.5	-9.8	1.4
Wipha & Francisco	Oct. 9-26, 2013	-8.7	1.4	-8.8	1.4
Phanfone & Vongfong	Sept. 28 - Oct. 14, 2014	-8.2	1.4	-8.4	1.4
Etau	Sept. 6 - 9, 2015	-7.2	1.5	-7.2	1.4

585
586
587
588
589
590
591
592
593
594
595
596
597
598
599

Figure captions

Figure 1. Spatial variability of the radiocaesium contamination plume in the eastern part of Fukushima Prefecture with locations of the 40 meteorological stations within a 100 km buffer around the FDNPP (dashed line) and the two investigated catchments (full black line). ^{137}Cs activities are decay corrected to March 11 2011 (Chartin et al., 2013)

Figure 2. Mean daily rainfall from the 40 meteorological stations located in the 100 km buffer around the FDNPP (Fig.1) from March 2011 to November 2015 (FW indicates field work sampling campaigns; tropical storms and typhoons are highlighted by the dashed arrows).

Figure 3. Elevation (A) and dominant land cover classes (B) for the Mano and Niida catchment.

Figure 4. Box-plots of ^{137}Cs contamination (in kBq kg^{-1}) in sediment sampled in Mano and Niida rivers after each typhoon season since the FDNPP accident ^{137}Cs activities are decay corrected to 11 March 2011; outliers were excluded from the datasets and the red dots in the box plots indicate the mean concentrations.

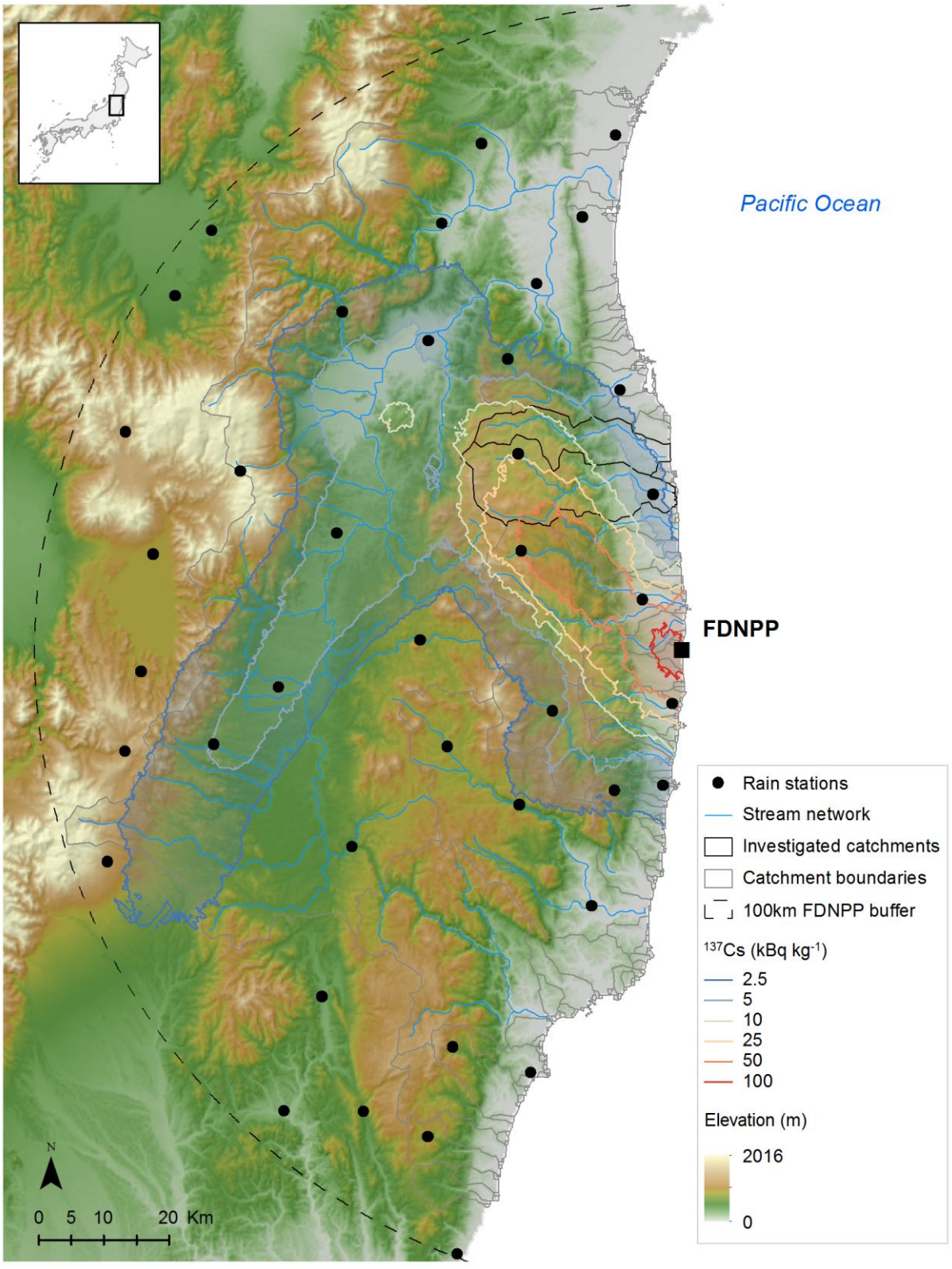
Figure 5. Sediment enrichment ratio (ER) values measured after each typhoon season since the FDNPP accident.

Figure 6. Rainfall erosivity (EI_{30} in MJ mm ha^{-1} h^{-1}) of the most intensive typhoons that occurred prior each sampling campaigns since the FDNPP accident for the catchments containing the main radioactive contamination plume (A) and for the two investigated catchments (B).

Figure 7. The revised connectivity index (ICrev) for the typhoons that occurred prior each sampling campaign since the FDNPP accident.

Figure 8. Relationships between the revised Index of Connectivity (ICrev) and the Enrichment Ratio values (ER*) for sediment sampled the Mano river (grey) and the Niida river (black).

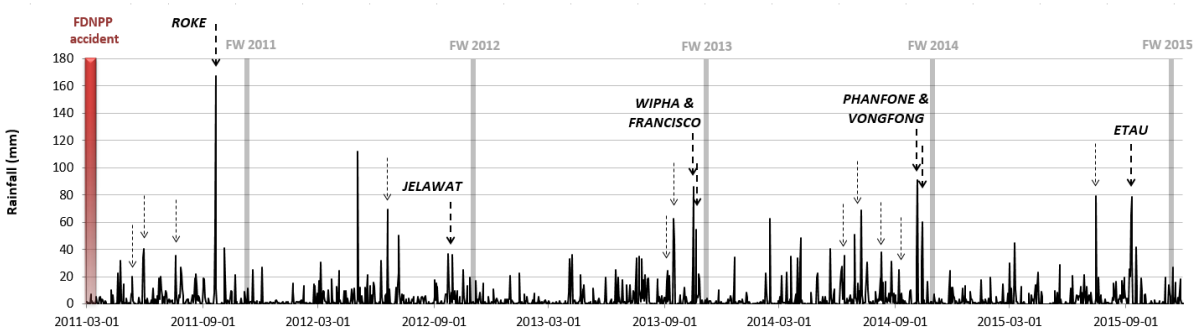
631 Figure 1.



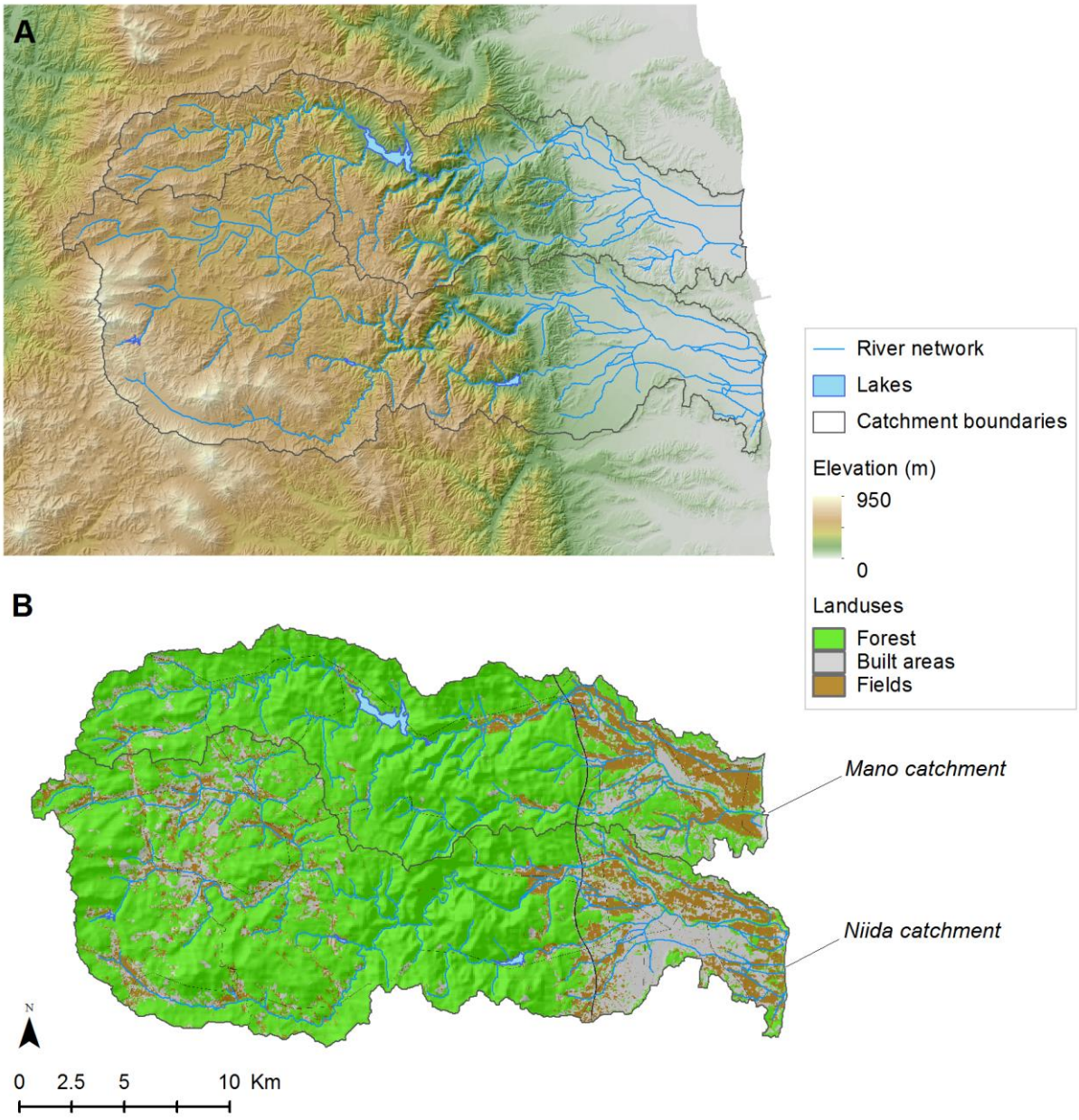
632

633

Figure 2.


FDNPP accident
ROKE
FW 2011
FW 2012
FW 2013
FW 2014
FW 2015
JELAWAT
WIPHA & FRANCISCO
PHANFONE & VONGFONG
ETAU
Rainfall (mm)
0
20
40
60
80
100
120
140
160
180
2011-03-01
2011-09-01
2012-03-01
2012-09-01
2013-03-01
2013-09-01
2014-03-01
2014-09-01
2015-03-01
2015-09-01

651 Figure 3



652

653

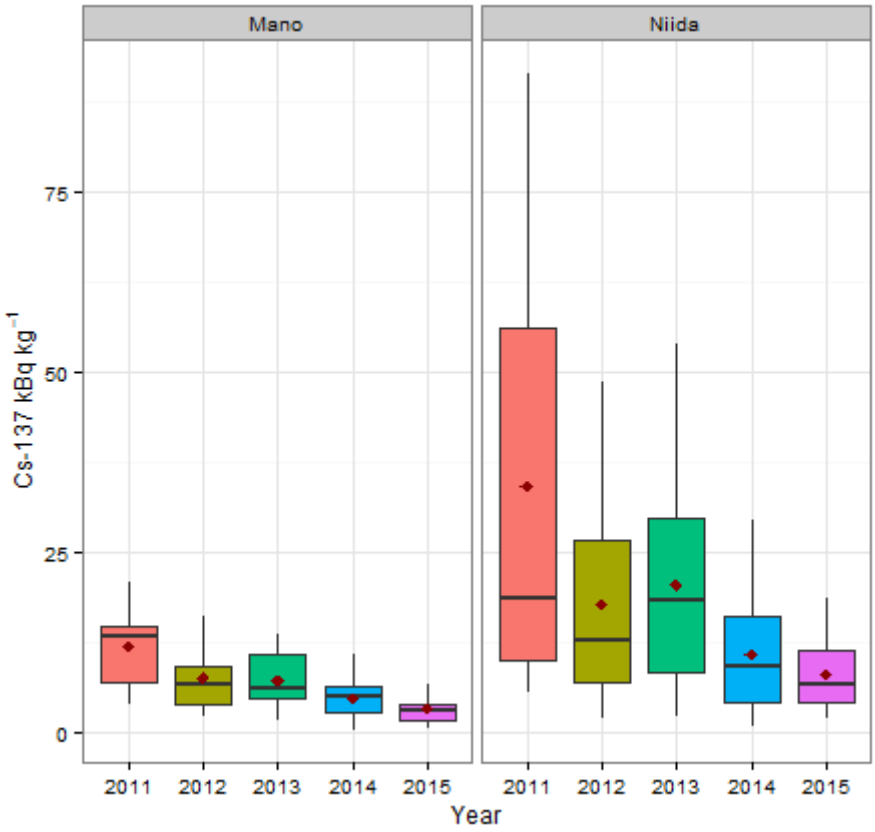
654

655

656

657

658 Figure 4.



659

660

661

662

663

664

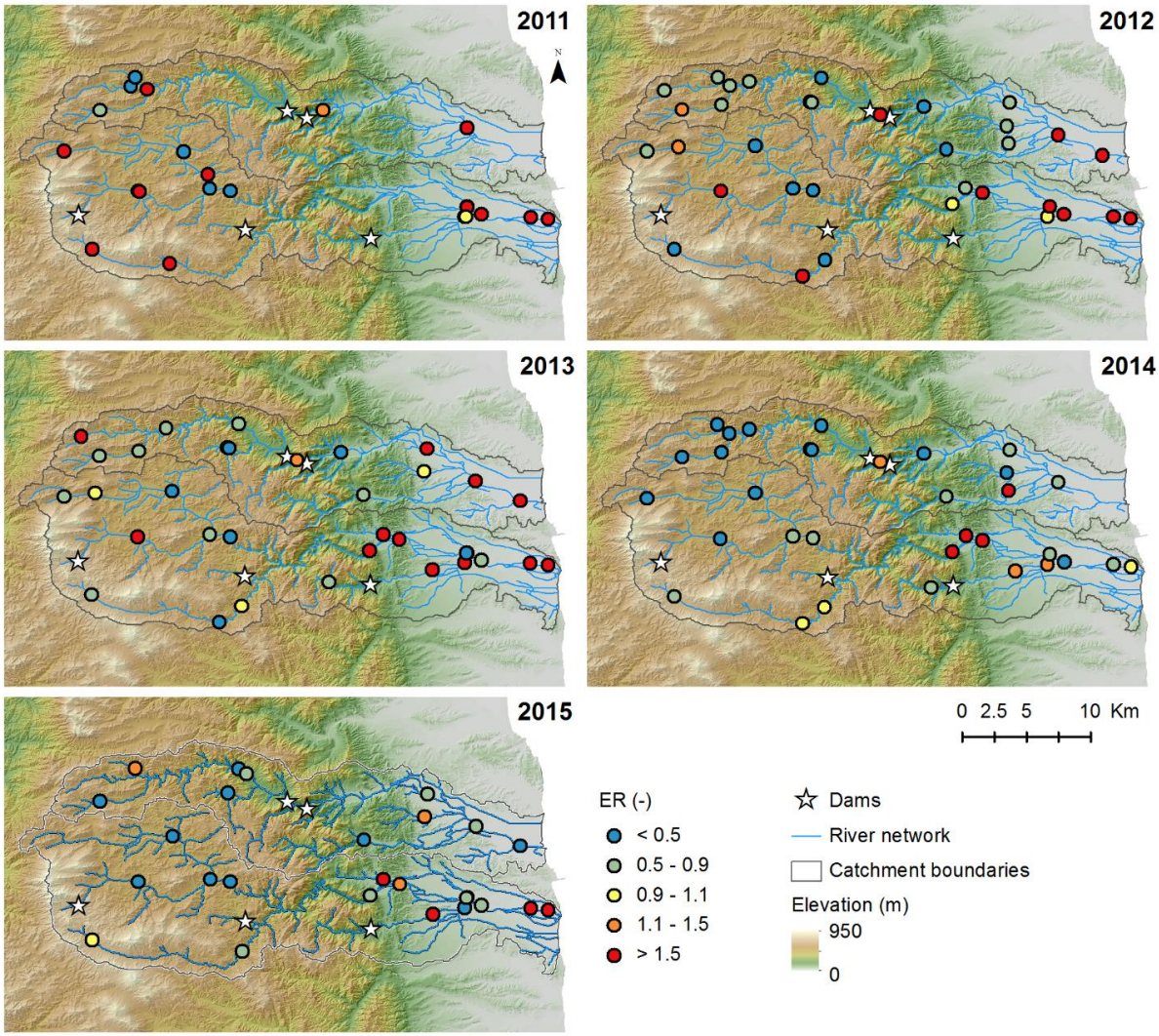
665

666

667

668

669 Figure 5.



670

671

672

673

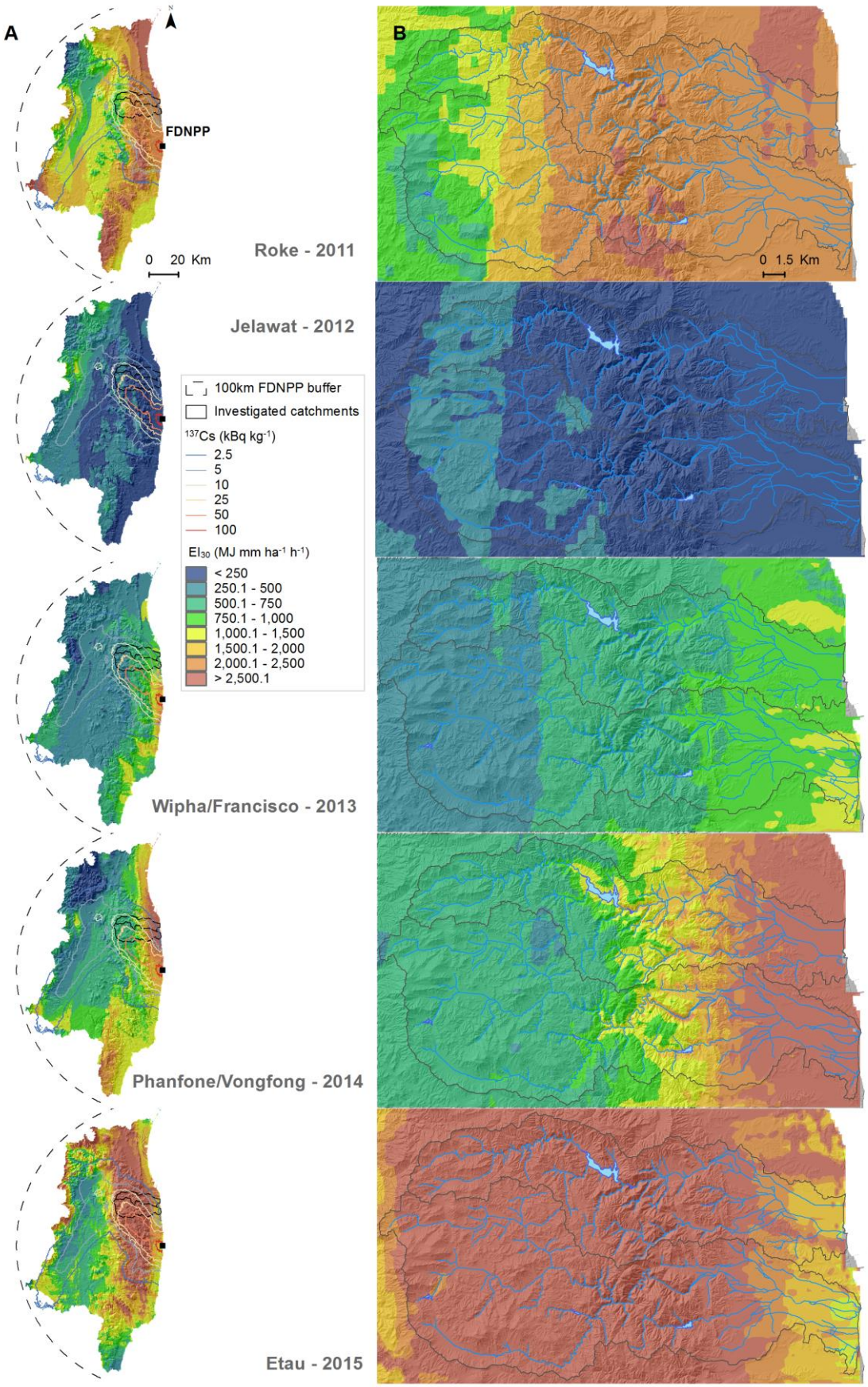
674

675

676

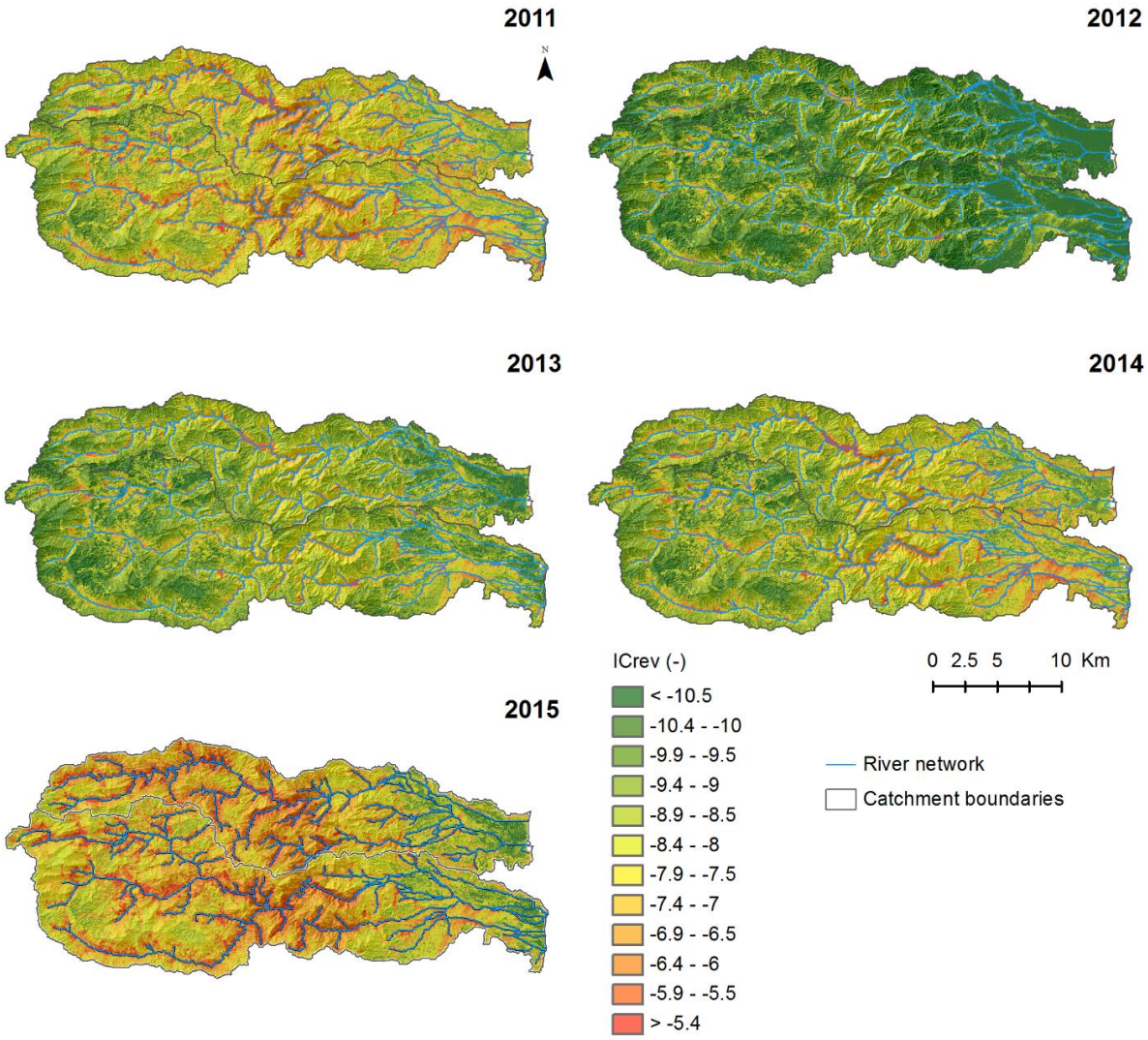
677

678 Figure 6.



679

680 Figure 7.



681

682

683

684

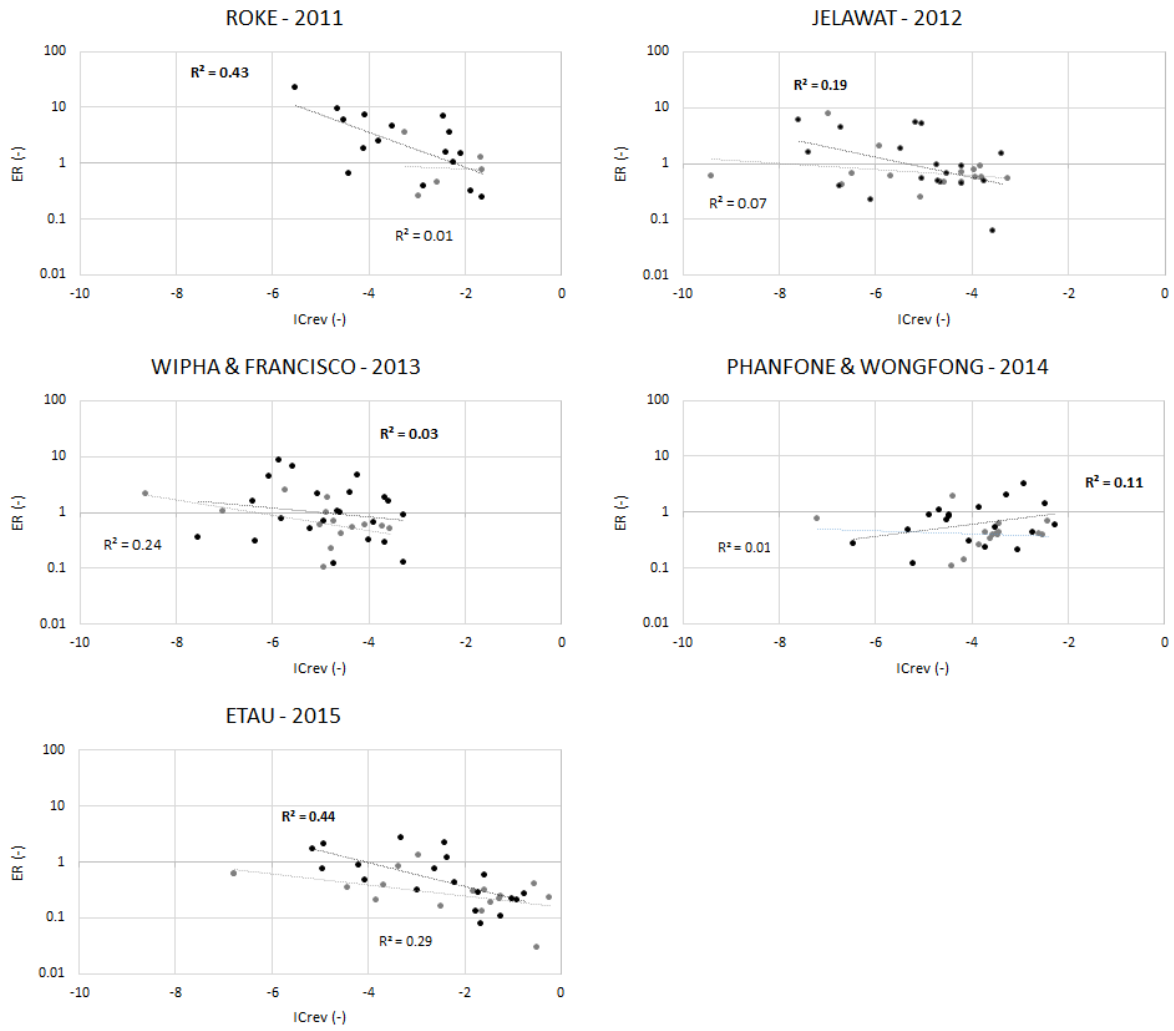
685

686

687

688

689 Figure 8.



690